

**The influence of the quasi-biennial oscillation on the Madden-Julian oscillation in idealized
cloud-resolving simulations**

Zane Martin¹

Shuguang Wang¹

Ji Nie²

Adam Sobel^{1,3}

1 Department of Applied Physics and Applied Mathematics, Columbia University, New York,
NY

2 Department of the Atmospheric and Oceanic Sciences, Peking University, Beijing, China

3 Lamont-Doherty Earth Observatory of Columbia University, Palisades, NY

Corresponding author: Zane Martin, zkm2102@columbia.edu

Draft to be submitted to
Journal of Atmospheric Sciences

2018

1 **Abstract:**

2 This study examines the relationship between the Madden-Julian oscillation (MJO) and the
3 stratospheric quasi-biennial oscillation (QBO) in a limited-area cloud-resolving model with
4 parameterized large-scale dynamics. The model simulates two consecutive MJO events that
5 occurred during the late fall and early winter of 2011. To test the influence of the QBO on the
6 simulated MJO events, various QBO states are imposed via the addition of characteristic QBO
7 wind and temperature anomalies to the large-scale environment. In experiments in which only
8 QBO temperature anomalies are imposed (without corresponding zonal wind anomalies) the
9 strength of convection during MJO active phases is amplified for the QBO easterly phase
10 (anomalously cold tropical tropopause layer, TTL) compared to the westerly QBO phase (warm
11 TTL), as measured by outgoing longwave radiation, cloud fraction, and large-scale ascent. This
12 response is qualitatively consistent with the observed MJO-QBO relationship. The response of
13 precipitation is weaker and less consistent across variations in the simulation configuration.
14 Experiments with imposed QBO wind anomalies only (without corresponding temperature
15 anomalies) show much weaker effects altogether than those with imposed temperature
16 anomalies. These results suggest that tropopause temperature anomalies are a key pathway
17 through which the QBO can modulate the MJO. Sensitivity tests indicate that the QBO influence
18 on MJO convection depends on both the amplitude and the height of the QBO temperature
19 anomaly: both lower altitude and larger amplitude temperature anomalies have a more
20 pronounced effect on MJO convection.

21 **1 Introduction**

22 The Madden-Julian oscillation (MJO) and stratospheric quasi-biennial oscillation (QBO) are
23 two prominent modes of variability in the tropical atmosphere. Likely because they occur on
24 different timescales and occupy largely distinct parts of the tropical atmosphere, the two
25 phenomena were considered independent by most until recent discoveries by Yoo and Son
26 (2016) and others showed a strong connection between the MJO and the QBO in boreal winter.
27 Here, we briefly introduce both phenomena, then discuss the newly discovered MJO-QBO
28 relationship and potential mechanisms explaining the connection.

29 The MJO is the dominant mode of intra-seasonal variability in the tropical troposphere and is
30 marked by a planetary-scale organization of deep convection and circulation (Madden and Julian
31 1994; Zhang 2005). Consisting of an “active” phase associated with increased convection and a
32 corresponding “suppressed” phase associated with decreased convection, the MJO propagates
33 eastward from the Indian Ocean through the West Pacific on timescales typically around 30 to 60
34 days. In contrast, the quasi-biennial oscillation (QBO) is the main source of inter-annual
35 variability in the tropical stratosphere (Baldwin et al. 2001). Its prevailing signal is an
36 approximately 28-month cycle in which the tropical stratospheric zonal wind reverses direction,
37 alternating between an easterly (QBOE) and westerly (QBOW) phase. These alternating easterly
38 and westerly regimes form in the upper stratosphere and descend to near the tropopause at a rate
39 of around 1 km/month. The QBO also possesses a clear temperature signal in both tropical and
40 extratropical regions that largely follows thermal wind balance (Baldwin et al. 2001).

41 A relationship between the QBO and the MJO was first noted by Kuma (1990), who found a
42 quasi-biennial signal in upper-tropospheric winds associated with the MJO that was well-
43 correlated with the QBO. While little subsequent work was done at the time, more recent studies,

44 beginning with Yoo and Son (2016), have spurred renewed interest in the topic (Yoo and Son
45 2016; Marshall et al. 2017; Son et al. 2017; Hood 2017; Nishimoto and Yoden 2017; Lee and
46 Klingaman 2018; Zhang and Zhang 2018; Hendon and Abhik 2018; Wang et al. 2018).

47 Yoo and Son (2016), through examining different QBO and MJO indices, found a strong
48 correlation indicating the boreal winter MJO is significantly stronger during QBOE and weaker
49 in QBOW. Notably, the correlation was not significant in other seasons. Son et al. (2017) and
50 Nishimoto and Yoden (2017) showed further evidence for the MJO-QBO link and described the
51 relationship in more detail through composite analyses of the MJO during different QBO phases.
52 These and other studies have found that during QBOE winters, the MJO tends to propagate
53 slower, last longer, and display stronger teleconnections (Son et al. 2017; Nishimoto and Yoden
54 2017; Marshall et al. 2017; Wang et al. 2018). Marshall et al. (2017) provided additional
55 evidence for a link between the MJO and QBO in a numerical weather prediction model and
56 showed that MJO prediction, as measured by the lead time at which the bivariate correlation of
57 an MJO index remained above 0.5, improved by approximately a week in QBOE versus QBOW.
58 Recently, Zhang and Zhang (2018) have argued that the QBO does not directly modulate the
59 strength of active MJO events; instead there are more active MJO days in QBOE and the MJO
60 propagates more frequently through the Maritime Continent, often lasting longer. While these
61 works demonstrate a link between the MJO and the QBO, none of these studies clearly
62 establishes the physical mechanism responsible for this link.

63 Several mechanisms have been proposed to explain the MJO-QBO connection, including the
64 QBO temperature stratification effect, cloud-radiative feedbacks, and the QBO wind shear effect.
65 The QBO temperature stratification effect is perhaps the most plausible (Hendon and Abhik
66 2018). It asserts that QBO temperature anomalies modify the thermal stratification in the

67 tropopause region, destabilizing the atmosphere during QBOE and promoting more vigorous
68 deep convection (and vice versa during QBOW). Previous work examining the QBO's effect on
69 tropical mean convection (not necessarily associated with the MJO) has also identified the
70 potential for temperature anomalies to modulate convection (Gray et al. 1992a, 1992b; Giorgetta
71 et al. 1999; Collimore et al. 2003; Garfinkel and Hartmann 2011; Liess and Geller 2012; Nie and
72 Sobel 2015).

73 In addition to the direct temperature stratification effect of the QBO, cloud-radiative
74 feedbacks have been suggested as a further driver of the MJO-QBO link. During QBOE, cold
75 temperatures near the tropopause are conducive to the formation of cirrus clouds at high
76 altitudes, whereas warm temperatures are less conducive (e.g. Son et al. 2017). These cirrus
77 clouds may feedback on existing temperature anomalies by cooling locally at high altitudes
78 while warming the atmosphere below (Hartmann et al. 2001; Yang et al. 2010; Hong et al. 2016),
79 potentially reducing the column-integrated radiative cooling and increasing large-scale ascent
80 and precipitation through moist static energy arguments (Nie and Sobel 2015). As cloud-
81 radiative feedbacks are potentially important to the maintenance of the MJO (e.g. Bony and
82 Emanuel 2005; Sobel and Maloney 2012, 2013; Creuger and Stevens 2015), this mechanism
83 seems particularly well-suited in explaining why MJO-related convection seems to be modulated
84 by the QBO more than tropical mean convection (e.g. Son et al. 2017, their Figure 1).

85 Another possible mechanism is related to QBO wind anomalies. Gray et al. (1992a, 1992b)
86 and Collimore et al. (2003) suggested that QBO wind anomalies may influence tropical
87 convection via changes to the vertical wind shear around the tropopause, which may shear off
88 convecting cloud tops or otherwise affect convection. Apart from these mechanisms, which
89 couple QBO anomalies to convection locally, QBO wind changes can be expected to alter the

90 propagation and dynamics of transient waves excited by the MJO, such as vertically propagating
91 gravity or Kelvin waves. Modulation of vertically propagating waves in the stratosphere by
92 varying vertical wind shear is a central part of the mechanism of the QBO itself (Lindzen and
93 Holton 1968; Holton and Lindzen 1972), and it is conceivable that such modulation could
94 influence waves down into the troposphere and play a role in the MJO-QBO interaction. Such
95 mechanisms are not examined in this work.

96 In this study we seek to model the MJO-QBO connection using a numerical model, and to
97 explore mechanisms that couple QBO temperature and wind anomalies directly to convection in
98 the local column. We simulate the MJO in a limited-area cloud-resolving model augmented with
99 parameterized large-scale dynamics, following Wang et al. (2013, 2016), and then examine the
100 impact of the QBO by imposing characteristic QBO anomalies in the simulation. One advantage
101 of this approach is that the use of cloud-resolving simulations avoids the large uncertainty due to
102 convective parameterization in climate models. Additionally, imposing QBO anomalies allows
103 us to focus on the QBO's impact on the MJO and avoid issues simulating the QBO itself, which
104 can cause difficulties in free-running global climate model simulations (e.g. Lee and Klingaman
105 2018). Furthermore, such an approach allows us to examine QBO temperature and wind effects
106 separately, which is a difficult in a climate model due to the thermal wind balance constraint.

107 Following the modeling study of Wang et al. (2016, hereafter "W16"), we begin by
108 simulating two consecutive, observed MJO events in our model. The specifics of our model
109 configuration, the data and techniques we utilize, and our experimental design are described in
110 Section 2. After establishing that our model reproduces with reasonable fidelity the two observed
111 MJO events, we conduct a series of QBO experiments, loosely following the experimental
112 design of Nie and Sobel (2015), to test whether QBO temperature anomalies and/or wind

113 anomalies influence the simulated convection. The results from these experiments are presented
114 in Section 3. Discussion of our results comprises Section 4, and a summary with our conclusions
115 is laid out in Section 5.

116

117 **2. Data, Methodology, and Model Configuration**

118 **2.1. Data and Parameterized Large-Scale Dynamics**

119

120 The observational data used in this study are from two sources: the Cooperative Indian
121 Ocean Experiment on Intra-seasonal Variability in the Year 2011/Dynamics of the Madden-
122 Julian Oscillation field campaign (CINDY/DYNAMO or simply DYNAMO) (Yoneyama et al.
123 2013) and the European Centre for Medium-Range Weather Forecasts’ global interim reanalysis
124 (ERA-Interim) (Dee et al. 2011). The DYNAMO data used here consist of six-hourly radiosonde
125 measurements from October 1, 2011 through December 15, 2011, averaged horizontally over
126 DYNAMO’s Northern Sounding Array (NSA). The NSA was a large region in the central
127 equatorial Indian Ocean marked by four sounding sites (Johnson and Ciesielski 2013; Sobel et al.
128 2014; Johnson et al. 2015). As the DYNAMO data do not extend above around 21 km, ERA-
129 Interim reanalysis is utilized to capture the state of lower to mid stratosphere up to around 29 km.
130 To combine these two data sets, the DYNAMO data are linearly merged with six-hourly ERA-
131 Interim data, which in turn are horizontally averaged over 0-6°N and 73-80°E, a region closely
132 corresponding to the NSA. Explicitly, at heights z between approximately 18km and 21km, a
133 generic variable, say $X(z)$, is expressed as $X(z) = X_{DYN}(z) \left(\frac{21-z}{21-18} \right) + X_{ERA}(z) \left(\frac{z-18}{21-18} \right)$, where
134 X_{DYN} and X_{ERA} are the horizontally-averaged values of X in the DYNAMO and ERA-Interim
135 data sets, respectively. This linear merging is done for both the wind and the temperature fields.

136 For ease of reference, this combined ERA-Interim/DYNAMO data set is referred to simply as
137 “the DYNAMO data.”

138 Several fields from the DYNAMO data are shown in Figure 1. During the fall and early
139 winter of 2011, two MJO events passed through the NSA. The active phases of these events are
140 evident both in the strong ascent through the troposphere and the increased precipitation centered
141 around days 25 and 55. Additionally, the suppressed phase from around days 30 to 50 shows
142 decreased precipitation and weak descent. Also notable in Figure 1 are the QBO signals in zonal
143 wind in the stratosphere: the QBO at 50hPa (~ 21 km) during this period was westerly in October
144 and November, and neutral by December 2011 (see further at Section 2.4).

145 The DYNAMO data is coupled to our cloud-resolving model following a method
146 outlined in W16. The key step is to derive the large-scale vertical velocity using the weak
147 temperature gradient approximation (“WTG”; Sobel and Bretherton 2000; Raymond and Zeng
148 2005; Sessions et al. 2010; Wang and Sobel 2011) discussed below, though the model is also
149 constrained by observations in other aspects. The horizontally-averaged model zonal and
150 meridional wind are relaxed uniformly at each model level towards the DYNAMO wind profile.
151 The lower boundary condition of the model is a horizontally uniform daily sea surface
152 temperature taken from OAFlux. Additionally, the large-scale horizontal advection of moisture is
153 specified by imposing an additional tendency term to the moisture budget consistent with the
154 observed horizontal moisture advection (Figure 1, panel d), forcing the model with significant
155 low-level drying associated with westerly-winds (Sobel et al. 2014).

156

157 **2.2. Spectral Weak Temperature Gradient based on Vertical Structure**

158

159 Limited-area cloud-resolving simulations are typically driven by prescribing the large-
 160 scale vertical wind and the vertical advective tendencies, a method that is useful for studying
 161 convective characteristics (Wang et al. 2015; Li et al. 2018). However, since specifying these
 162 fields misrepresents causality related to convection and circulation (Mapes 1997, 2004), methods
 163 exist to parameterize the large-scale vertical velocity and vertical tendencies (e.g. Sobel and
 164 Bretherton 2000; Raymond and Zeng 2005; Kuang 2008; Romps 2012a, 2012b; Wang et al.
 165 2013; Herman and Raymond 2014; Edman and Romps 2015; Nie and Sobel 2016; W16) and an
 166 intercomparison with many different models in idealized simulations can be found in Daleu et al.
 167 (2015, 2016). Following W16 and Herman and Raymond (2014), we utilize one such technique,
 168 known as the vertical-mode based, spectral weak temperature gradient method (SWTG).

169 Weak temperature gradient methods make use of the fact that horizontal temperature
 170 gradients in the tropical troposphere are small because local temperature anomalies are quickly
 171 removed by gravity waves. The WTG method assumes that the large-scale vertical velocity, w ,
 172 maintains this homogeneity in temperature by restoring the virtual potential temperature, θ , to
 173 some reference profile θ_{ref} . Mathematically, this can be represented via a truncation of the
 174 temperature equation as:

$$\bar{w} \frac{\partial \bar{\theta}}{\partial z} = \frac{\bar{\theta} - \bar{\theta}_{ref}(z,t)}{\tau} \quad (1),$$

175
 176
 177 where the overbar indicates horizontal averaging. Here τ is a relaxation time scale, usually on the
 178 order of hours, associated with how quickly gravity waves propagate through the domain. τ is
 179 thus inversely proportional to the gravity waves' phase speeds. Note that here our reference
 180 virtual potential temperature profile is a function of height, as is typical, but is also time
 181 dependent. While this is not often the case in idealized WTG experiments, several recent studies

182 have demonstrated its viability (e.g. Wang et al. 2013, Sentic et al. 2015, W16). Within the
183 model, Equation (1) is solved for w throughout the free troposphere, and the resulting large-scale
184 or WTG vertical velocity is used to advect moisture and temperature.

185 Here we use the spectral weak temperature gradient method developed by Herman and
186 Raymond (2014) as modified by W16. We solve Equation (1) by first decomposing the vertical
187 velocity as a sum of vertical modes, each with an associated vertical structure and phase speed.
188 We then assume that WTG holds individually for each mode, and further that the i th mode has a
189 characteristic time-scale, say τ_i , inversely proportional to its phase speed. This assumption is
190 based on the fact that a hydrostatic gravity wave's phase speed depends only on its vertical
191 wavelength, so that various vertical modes may have different timescales. W16 showed that
192 these modes could be calculated from the vertical profile of the Brunt-Vaisala frequency by
193 solving a vertical structure equation with specified boundary conditions (W16 Section 2.2.3), a
194 technique that has often been applied to studies of the tropical atmosphere (e.g. Fulton and
195 Schubert 1985; Wu et al. 2000; Bergman and Sardeshmukh 2004; Mapes 2004; Tulich et al.
196 2007). Once the modes are calculated, the right-hand side of Equation (1) is projected onto the
197 vertical modes, and the large-scale vertical velocity field is then obtained by solving Equation (1)
198 for each mode and then summing over the modes to obtain the total w .

199 We utilize this vertical-mode based SWTG methodology both because it is conceptually
200 appealing and because it produces smooth vertical velocity profiles. Additionally, W16 showed
201 that this parameterization leads to the most realistic simulations of the DYNAMO MJO events
202 compared to other large-scale parameterizations. Here, the N^2 profile used to calculate the
203 modes is the time-mean from the DYNAMO data. We calculate the first 20 modes, assuming a

204 rigid lid boundary condition in the vertical velocity at 20 km. The sensitivity to the rigid lid
205 height is explored in Appendix A where it is set to 16 km in a separate set of experiments.

206

207 **2.3. Numerical Model and Forcing**

208

209 Our cloud-resolving simulations use the WRF model V3.5.1 (Skamarock, et al. 2008).
210 The set-up largely follows W16 and is broadly similar to other WTG studies (e.g. Wang et al.
211 2013, Sentic et al. 2015; Edman and Romps 2014). The horizontal domain is 64 by 64 km with a
212 1 km resolution and doubly periodic lateral boundary conditions. To better represent the lower
213 stratosphere, we improve upon W16 by extending the model top to around 29 km with 89
214 vertical levels (from the ~22 km used in W16). Following Nie and Sobel (2015), these levels are
215 not uniformly spaced, but vary to include more levels near the surface and the tropopause. There
216 are 20 levels below 5 km with a linearly-increasing step size from 75 m to 500 m; above 5 km
217 the resolution is 500 m, except from 12 km to 20 km where it is decreased to 250 m.

218 We use the Morrison microphysics scheme, which predicts the mixing ratio and number
219 concentration of water vapor, rain, cloud water, cloud ice, snow, and graupel (Morrison 2009).
220 The radiative fluxes are calculated within the model via the RRTMG longwave scheme (Iacono
221 et al. 2008) and the Goddard shortwave scheme (Chou and Suarez 1999; Matsui et al. 2007; Shi
222 et al. 2010). The solar constant at 76°E 3°N is specified uniformly over the domain for
223 calculation of shortwave radiative fluxes and includes the diurnal cycle. An implicit damping
224 vertical velocity scheme is used in the top 6 km of the model domain to suppress gravity wave
225 reflection off the top boundary (Klemp et al. 2008). Subgrid scale turbulent mixing eddies are
226 parameterized using the 3-D Smagorinsky first-order closure scheme. To ensure conservation of

227 moisture, we utilize the implicit vertical diffusion scheme from W16 and similar to Hong et al.
228 (2006). The Coriolis parameter is set to zero, as the NSA is close to the equator and the domain
229 is small relative to the equatorial deformation radius. The model simulation is sampled four-
230 times daily.

231 Following W16, all runs are initialized on October 10, 2011. In runs initialized on
232 October 1, the model settles into an unrealistically dry state with no precipitation. This sensitivity
233 to initial moisture leading to “multiple equilibria” has been found in other WTG simulations
234 (Sobel et al. 2007; Session et al. 2010). Examining the transition behavior of w in such states
235 suggests that the dry equilibrium originates from an ascent/descent couplet in the middle
236 troposphere (e.g. day 10 in Figure 3, panel d; Anber et al. 2017). This couplet grows and
237 descends because of interaction between radiation-driven warm anomalies and WTG (Mapes and
238 Zuidema 1996; Emanuel et al. 2013). More importantly, it removes moisture from the column,
239 and the system settles into the dry state. In our tests, initialization on October 10 avoids this issue
240 in many of our simulations, though non-precipitating states occur in some experiments discussed
241 below. Model initial conditions of moisture, temperature, winds, and geopotential heights are
242 created with an observed sounding averaged over the NSA and including ERA-Interim data in
243 the lower stratosphere. To break symmetry, uniformly distributed random noise of magnitude 2
244 K is added to the initial potential temperature field in the bottom ten levels. This also permits us
245 to carry out ensemble integrations to better distinguish signal from noise.

246 Also following W16, the reference profile of virtual potential temperature ($\bar{\theta}_{ref}$) is not
247 taken directly from the DYNAMO data but instead is calculated from a model run with imposed
248 vertical velocity, as this leads to better simulations because unavoidable model bias is explicitly
249 taken into account (Edman and Romps 2014; W16). The domain-averaged horizontal wind

250 profiles are relaxed to the NSA fields with a one-hour relaxation. The SWTG relaxation
251 timescale, τ , is also set to one hour.

252 Finally, because our model top is higher than in W16, two additional modifications were
253 made from their study. First, the temperature and winds in the stratosphere are relaxed towards
254 the reference virtual potential temperature above 20 km (i.e. above where the SWTG vertical
255 velocity is calculated) to prevent unrealistic drift. Additionally, large-scale horizontal advection
256 of moisture above 15 km is set to zero, as in some integrations small amounts of imposed drying
257 lead to unphysical negative moisture values. As the actual forcing is already near zero at these
258 levels, this change has a negligible effect on the simulations where no negative moisture
259 anomalies develop.

260

261 **2.4. Experimental Design**

262

263 We track the QBO using ERA-Interim monthly zonal-mean zonal wind at 50hPa (U50),
264 averaged over the tropics (10°N-10°S and all longitudes) from January 1979 to June 2017.
265 Months when U50 is greater than or less than half of its standard deviation are defined as QBOW
266 and QBOE, respectively. During the DYNAMO period, the QBO was westerly during October
267 and November and neutral by December 2011. It should also be noted that the DYNAMO events
268 studied here occurred in the fall and early winter, whereas the observed MJO-QBO relationship
269 seems limited to December-February. Despite both the existing QBO state and the season, we
270 treat the simulated DYNAMO MJO events as a “control” case. This is justifiable in part because
271 we are primarily interested in the relative QBO changes to the MJO, and the DYNAMO period
272 captured two reasonably strong MJO events.

273 We now describe the QBO anomalies we impose upon the control simulation. We first
 274 composite vertical profiles of tropical-averaged zonal-mean temperature and wind in QBOE and
 275 QBOW. The anomaly relative to the time-mean temperature and wind from ERA-Interim
 276 monthly data are plotted in Figure 2. Following Nie and Sobel (2015), we then create idealized
 277 temperature and wind anomalies as parabolas with a peak amplitude approximately equal to the
 278 observed QBO signal, written as:

$$279 \quad A_{u,t}'(z) = \begin{cases} \pm M_{u,t} \left[1 - \left(\frac{z-z_0}{H} \right)^2 \right] & \text{if } z_0 - H < z < z_0 + H \\ 0 & \text{otherwise.} \end{cases} \quad (2)$$

280 Here $A_{u,t}'$ is the anomaly, $M_{u,t}$ is the amplitude of the anomaly, and the subscript denotes zonal
 281 wind or temperature. The \pm indicates positive or negative anomalies, though in some cases the
 282 magnitude of the QBOE and QBOW anomalies are not symmetric. For the QBO wind anomalies
 283 in this paper, the values of M_u used are -15 m/s and 10 m/s for QBOE/W respectively. For the
 284 temperature anomalies, the values of M_t are symmetric and are either ± 1 K, ± 0.5 K, or ± 2 K,
 285 where indicated in the sections below; in most runs $M_t = \pm 1$ K. The anomaly peaks at height z_0 ,
 286 and it is symmetric in the vertical between $z_0 - H$ and $z_0 + H$, so that H is the half depth of the
 287 QBO anomaly. The peak height of the anomaly varies across different runs: QBO temperature
 288 anomalies have z_0 ranging from 16 km to 20 km, and QBO wind anomalies vary z_0 from 18km
 289 to 22km, in both cases in 1 km increments. Across all our experiments, while M_t and z_0 are both
 290 varied, the half depth is fixed at $H = 4$ km. Note that observed QBO signals in the middle to
 291 upper stratosphere are not included in our idealized anomalies, as it seems unlikely that such
 292 high-altitude anomalies could affect convection (see **Section 3.3** for validation).

293 To impose the idealized QBO states, we add the QBO anomaly to the DYNAMO large-scale
 294 forcing data during the entire simulation period. While the observed QBO anomalies descend at

295 a rate of around 1 km/month, our anomalies are fixed in altitude. The QBO anomalies were
296 further not added to the initial conditions: simulations in which the model was initialized with
297 QBO anomalies in some cases lead to the model settling into the non-precipitating state
298 discussed above. While this itself suggests that conditions around the tropopause region can
299 impact on MJO-related convection, these states preclude comparison to other runs and do not
300 simulate the MJO realistically.

301 We design three types of experiments to test the mechanisms discussed in the introduction:
302 those in which only the large-scale temperature field is modified via addition of QBOE/W
303 signals, those where only the large-scale wind is modified, and the final type where QBO
304 temperature and wind signals are both added. In each set of experiments, we add both QBOE and
305 QBOW anomalies, looking at the changes they result in both relative to one another and to the
306 control. To account for ambiguity in the height and amplitude of the anomalies, and to explore
307 sensitivity to these parameters, we considered a range of heights and amplitudes for our idealized
308 anomalies. These sensitivity tests are conducted in Section 3.3. A summary of all the
309 experiments presented in this paper, as well as the section in which they are discussed, is
310 provided in Table 1.

311

312 **3. Results**

313 **3.1. Control Runs**

314

315 Our control runs are comparable to W16's simulations with interactive radiation (their
316 Section 3.2), albeit with a higher model top and higher vertical resolution. Figure 3 shows the
317 results from control simulations with five ensemble members, with spread due to the white noise

318 in the initial temperature field. Comparisons of the model and observations in Figure 3 shows
319 that the control runs simulate the two MJO active phases with reasonable fidelity. The model
320 reproduces both periods of increased precipitation associated with the MJO active phases, though
321 the large spike in precipitation around day 55 is missed and the second MJO event develops later
322 in the model than in the observations. The dry, suppressed phase is also well-realized in the
323 model, evident from around day 30 to day 55. In addition to the precipitation, the SWTG vertical
324 velocity is in fairly good agreement with the observed: the model captures the periods of ascent
325 during the active phases and the weak descent in the suppressed phase, although the magnitude
326 of the SWTG vertical velocity is often larger than the observed and the structure is more top
327 heavy. Note the model displays a descending couplet (ascent in the upper troposphere and
328 descent in the lower stratosphere) around day 45: this feature is inconsistent with the
329 observations during this period and can lead to unusually strong precipitation and/or low OLR.
330 W16 and Anber et al. (2017) noted this feature in their simulations with interactive radiation as
331 well.

332 Unlike the precipitation and vertical velocity, the model OLR differs more substantially
333 from the observations. Especially during the first MJO event, the model OLR disagrees with the
334 observations at times by tens of W/m^2 . The OLR during the second MJO event is in closer
335 agreement with the observations, though again the model MJO active phase begins later than the
336 observed. The OLR also has an unrealistic dip in the model around day 40-45 corresponding to
337 the descending couplet. Despite the discrepancies, we conclude that the model can reproduce the
338 observed MJO events reasonably well; our results are not substantially different from W16
339 despite the fact that we extended the model top and utilized slightly different SWTG vertical
340 modes.

341

342

3.2. QBO Experiments

343

344

345

346

347

348

In this section we present results from simulations in which we impose various QBOE and QBOW anomalies. We begin by only modifying the temperature field, before discussing the wind-only experiments and then the combined wind and temperature simulations. We first impose a QBOE/W anomaly with amplitude $M_t = 1$ K, with a peak z_o at 16 km, extending down to 12 km and up to 20 km. These QBOE and QBOW idealized anomalies are shown in Figure 2.

349

350

351

352

353

354

355

It should be stressed that the idealized temperature anomalies in this section are lower in altitude by around 2.5 km compared the observed and have a larger vertical depth, H . The sensitivity is explored more in Section 3.3, but in brief, it is likely that both the QBO forcing and the model response in these runs are stronger than in observations. We nevertheless include this stronger QBO temperature forcing in large part because of the clearer MJO response shown below, despite that fact that it seems inconsistent with observed QBO anomalies. Sections 3.3 and 4 discuss this issue in more detail.

356

357

358

359

360

361

362

363

As with the control, these QBOE and QBOW simulations are each performed with five ensemble members. The results are shown in Figures 4-6. These temperature-only experiments generally demonstrate an MJO response to the QBO that is qualitatively consistent with the observations: the model shows an increase in the strength of convection during the easterly phase of the QBO compared to the westerly phase. Figure 4 shows the time series of OLR and precipitation for the three QBO states: QBOE, QBOW, and the control. The OLR is consistently lower (higher) in QBOE (QBOW), while the precipitation is higher in QBOE and lower in QBOW: both are in keeping with enhanced convection during QBOE. The large-scale vertical

364 velocity and cloud fraction from these integrations are also consistent with stronger MJO
365 convection during QBOE, per Figure 5. The time-mean quantities show a significant change in
366 the amplitude of the vertical velocity throughout the troposphere from around 5km to 15km, such
367 that the vertical velocity is stronger during QBOE and weaker during QBOW. The same can be
368 said of the cloud fraction; the changes to high clouds in particular are in keeping with the
369 observed MJO-QBO interaction (e.g. Son et al. 2017). Figure 5 also shows a downward sloping
370 pattern in the QBOE-QBOW changes to cloud fraction, indicating that changes to high clouds
371 precede deeper, mid-tropospheric cloud changes (e.g. days 20-25 and days 45-55).

372 Across all variables, the time series show that QBOE-QBOW differences are most
373 pronounced during the MJO active phases: such differences are typically small or near zero
374 during the suppressed phase. This suggests, as one might expect, that only convection capable of
375 reaching the level of the QBO anomaly is modulated by the temperature changes. The
376 pronounced changes in the active phase and lack of change in the suppressed phase also
377 demonstrate that in these simulations QBO temperature anomalies modulate not only in the mean
378 state, but the amplitude of the variability associated with the MJO, as discussed more below.

379 Figure 6 shows the ensemble-averaged QBOE-QBOW potential temperature difference
380 in the simulations compared to the idealized QBO temperature anomaly (note here we plot
381 potential temperature, not temperature as in Figure 2). The model potential temperature
382 difference in the time mean is stronger (i.e. more negative) than the input anomaly around the
383 tropopause by around 0.4 K, which amounts to $\sim 10\%$ of the time mean value. This suggests that
384 some process in the tropopause region acts to enhance the existing QBO anomaly. The time
385 series in Figure 6 further shows that these enhanced temperature signals are largest during MJO
386 active phases, as evident around day 20-30 and day 50-60 where difference reach a minimum of

387 around -13 K, which is more than three times the imposed QBOE-QBOW potential temperature
388 difference of -4 K. These results show that the imposed QBO temperature anomalies enhance
389 coupling between large-scale velocity and convection, which in turn reinforce the QBO
390 temperature anomalies. It is possible that cloud-radiative processes during the active phase of the
391 MJO in the tropopause region play a crucial role in this feedback, which if true lends credence to
392 the hypothesis that such feedbacks are important in explaining the MJO-QBO relationship. These
393 results are also in keeping with Hendon and Abhik (2018), who examined the MJO's vertical
394 structure under different phases of the QBO and found that the cold cap around the tropopause
395 associated with the MJO is strengthened by around 0.5 K during QBOE, and similarly weakened
396 during QBOW.

397 In contrast to the QBO temperature-only simulations, results from experiments in which
398 the wind field was modified with QBO anomalies showed no substantial change across any of
399 the fields of interest, even for lower-than-observed altitude anomalies. Further evidence that
400 wind anomalies have little to no effect on convection is evident in the combined wind and
401 temperature experiments, in which QBO anomalies in both variables were added. Results from
402 these experiments are very similar to the temperature-only experiments, with minor differences
403 that are indistinguishable from noise. Because these differences are small in general, results from
404 both the wind-only and the temperature and wind results are not shown in detail but are
405 presented briefly in the following section (see Figures 7 and 8). This lack of an influence
406 suggests that QBO wind anomalies do not have a direct influence on MJO convection.

407

408 **3.3. Sensitivities to the Shape of QBO Temperature Anomaly**

409

410 In this section we explore the sensitivity of our results to the height and amplitude of the
411 QBO temperature anomaly. As in Nie and Sobel (2015), both parameters are found to be
412 important in determining the strength of the QBO influence on the simulated MJO. We also
413 briefly present results from the QBO wind-only and QBO wind and temperature experiments to
414 contrast their relatively small effect on the MJO with that of the temperature-only experiments.

415

416 **3.3.1. Height of the QBO Anomalies**

417

418 We first perform a series of one-member integrations in which the height of the QBO
419 anomalies in wind and temperature are varied in 1 km increments. QBO temperature anomalies
420 in these simulations have peak heights z_0 from 16 km to 20 km and QBO wind anomalies vary
421 z_0 from 18 km to 22 km. The vertical width of the anomaly H in all cases is 4 km; the observed
422 width of the anomaly tends to become thinner as it descends to lower levels, but for simplicity
423 we hold it fixed. The amplitude of the anomalies are also held fixed at 1 K for temperature and at
424 -15 m/s or 10 m/s for QBOE/W wind. When imposed together, the wind anomaly peaks 2 km
425 above the temperature anomaly, roughly consistent with the observed peak-height difference per
426 ERA-Interim. Figures 7 and 8 show the results of the integrations.

427 Figure 7 shows QBOE-QBOW difference in time-mean large-scale vertical velocity and
428 cloud fraction for various experiment types and values of z_0 . Immediately apparent in these
429 integrations is the similarity between the temperature-only simulations and temperature and wind
430 simulations, as well as the lack of a QBO signal in the wind-only runs. Of more interest is the
431 relationship between the height of the QBO temperature anomaly and the MJO response. These
432 experiments clearly show the QBO influence lessens dramatically as the height of the QBO

433 anomaly increases; changes to both cloud fraction and vertical velocity decrease and eventually
434 seem near zero in the runs with z_0 equal to 19 km and 20 km. The run with $z_0 = 18$ – the lowest
435 peak height for which the idealized anomaly is comparable to the observed QBO signal – is
436 subtler to diagnose and is discussed in more detail below. In addition to the weakening of the
437 QBO influence as z_0 increases, note that the peak of the QBOE-QBOW difference in vertical
438 velocity and cloud fraction shifts upward for higher anomalies and signals in the mid to lower
439 troposphere weaken. This suggests the QBO influence is increasingly confined locally as the
440 temperature anomaly moves to higher altitudes.

441 Figure 8 shows the QBOE-QBOW differences in the time mean and standard deviation of
442 precipitation and OLR as functions of z_0 for the three types of QBO experiment. The x -axis
443 indicates the height of the anomaly's peak and the y -axis indicates the QBOE-QBOW difference.
444 The OLR results are fairly consistent with the cloud fraction and vertical velocity changes
445 described above: there is a small change in the wind experiments, a similarity between the
446 temperature-only and the temperature and wind experiments, and a monotonic relationship
447 between the height of the QBO anomaly and the strength of the MJO convective response. This
448 is true both in the time mean and standard deviation.

449 Unlike the other variables, precipitation changes display a less clear or consistent
450 relationship as z_0 is varied. Only in the lowest altitude ($z_0=16$ km) temperature-only experiment
451 are precipitation signals clearly seen in the time mean or standard deviation. In all the higher-
452 altitude experiments from $z_0 = 17$ km upwards, it is difficult to detect a clear QBO-induced
453 signal in precipitation and it displays a lack of monotonicity. We conclude that no precipitation
454 signal is clearly present in these QBO experiments. Why the relationship seems clear for most

455 variables, but more nuanced for precipitation is discussed more in Section 4 in the context of
456 previous modeling and observational work.

457 To further explore forcing the model with more realistic altitude QBO anomalies, we
458 repeat the 18km-peaked temperature anomaly runs including more ensemble members. This
459 allows us to better assess the strength of the signal in the case where the MJO response is small.
460 As with the 16km-peaked runs in the previous section, we include five ensemble members each
461 for QBOE and QBOW. The results are shown in Figures 9-11.

462 Compared to the 16 km runs, the changes in the model to the 18km-peaked QBO
463 temperature anomaly are at times difficult to distinguish from noise. In precipitation in particular
464 (Figures 9 and 11), there no longer seems to be a robust or recognizable QBO signal in the mean
465 or in the time series. The QBO influence on OLR, while also much smaller than in the 16km-
466 peaked temperature experiments, is more consistent across ensemble members, and typically
467 shows a decrease during the MJO active phases in QBOE relative to QBOW, as well as a small
468 increase in the suppressed phase. Both vertical velocity and cloud fraction changes are clearer
469 than OLR or precipitation and are especially evident during MJO active phases. In the time-
470 mean, the changes have the same sign 16km-peaked results, albeit with a smaller magnitude
471 (Figure 10). In addition to a smaller in magnitude, the signal compared to the 16 km run is more
472 localized to the upper troposphere and is near zero below ~ 10 km in both cloud fraction and
473 vertical velocity.

474 Figure 11 compares the ensemble QBOE-QBOW spread in the time mean and standard
475 deviation of OLR and precipitation between the 16km-peaked and 18km-peaked runs. This
476 establishes that while time-mean QBOE precipitation is always higher than QBOW precipitation
477 in the 16km-peaked runs, the ensemble spread is fairly large; and the signal is absent in the

478 18km-peaked simulations. The time-mean QBOE-QBOW OLR changes across ensemble
479 members are also near zero in the 18km-peaked integrations. However, the 18 km runs do
480 display a signal in the standard deviation of OLR, with an ensemble-mean QBOE-QBOW
481 difference in standard deviation of approximately $5 W/m^2$ (Figure 11 panel d). In this regard,
482 the 18km-peaked runs may be more consistent with the observed relationship, with a small
483 change in the mean but a larger signal in the standard deviation (e.g. Son et al. 2017). However,
484 care should be taken in over-interpreting this result, as it may simply be fortuitous and
485 attributable to the small sign of the changes or the short time period over which we are
486 integrating. Additionally, this result is complicated by the fact that the OLR is not in good
487 agreement with observations to begin with, especially during the suppressed phase.

488

489 **3.3.2. Amplitude of the QBO Temperature Anomalies**

490

491 In this section we examine the effect of changing the amplitude of the QBO temperature
492 anomalies. We repeat the simulations from Section 3.2 where $z_0 = 16$ km but include additional
493 experiments either doubling or halving QBO temperature anomaly. Each experiment is
494 conducted with a single ensemble member. The results (Figures 12 and 13 and Table 2) indicate
495 a monotonic relationship between the amplitude of the QBO temperature anomaly and the
496 strength of the MJO convective response. The QBOE integrations with approximately double the
497 observed amplitude ($M_t = -2 K$) demonstrate the lowest OLR, strongest vertical velocity, and
498 highest cloud fraction. Similarly, the strongest QBOW integration ($M_t = 2 K$) shows the highest
499 OLR, the weakest vertical velocity and cloud fraction, and the lowest precipitation. The QBOE-
500 QBOW temperature anomalies with $M_t = \pm 0.5 K$ by contrast have the weakest response relative

501 to the control, while the “realistic” amplitude temperature anomalies with $M_t = \pm 1 K$ have a
502 response in between the $\pm 0.5 K$ and $\pm 2 K$ results.

503 While the time-mean precipitation response is monotonic (Table 2), the time series in
504 Figure 12 shows that precipitation generally varies in a more complex manner across these
505 integrations. The 2 K QBOE run, for example, rarely rains more than the 1 K and 0.5 K QBOE
506 runs, except in the periods following the MJO active phases, when observations suggest
507 precipitation ought to be lower. More significantly, the 2 K QBOW run completely misses the
508 second MJO event, settling into a dry, non-precipitating state discussed in Section 2.3 (see
509 precipitation Figure 12 at day 45). While this is inconsistent with the DYNAMO data and
510 prohibits comparison to some degree, it is indicative of the ability of temperature in the TTL
511 region to exert an influence on the troposphere (if too strongly so). That the precipitation time
512 series across these experiments are less monotonic than other variables is consistent with
513 findings already noted.

514

515 4. Discussion

516 Our results suggest that QBO-induced temperature anomalies in the tropical tropopause
517 region can influence convection associated with the MJO, providing a likely pathway for the
518 MJO-QBO relationship seen in observations. Our sensitivity experiments demonstrate that the
519 height and amplitude of the QBO temperature anomaly substantially affect the strength of the
520 MJO convective response. These sensitivities are consistent qualitatively with Nie and Sobel’s
521 (2015) results on the QBO influence on convection in statistically steady state, though their focus
522 is on convective equilibrium and not the MJO per se. The pronounced sensitivity to the height of
523 the temperature anomaly, as well as the fact that the model response to the QBO is primarily

524 during the MJO active phases, suggests that for the QBO to exert an influence on convection in
525 the troposphere, such convection must be deep enough to reach the region in which the QBO has
526 an impact. This is in keeping with other studies which show the QBO modulates convection in
527 regions where such convection is already strong (e.g. Collimore et al. 2003; Liess and Geller
528 2012). It may also offer insight into why the MJO-QBO link only manifests in boreal winter, as
529 MJO convection is known to be strongest during that season (e.g. Zhang 2013)

530 In addition to sensitivity to the QBO anomaly's height, our results show a sensitivity to
531 the amplitude of the QBO temperature anomaly. This finding may be particularly applicable to
532 the recent work by Lee and Klingaman (2018), who examined the MJO-QBO relationship in a
533 GCM and found no significant link between the two phenomena. One of their hypotheses was
534 that the GCM-simulated QBO temperature anomalies were too weak: less than one-fourth the
535 magnitude of the observed anomaly (their Figure 4). Our results here lend additional support to
536 that hypothesis.

537 As seen in Section 3.3 and below in Appendix A, the response of MJO-related precipitation
538 to the QBO state in our model is sensitive to the model configuration and displays less
539 monotonicity than other variables both as the height and amplitude of the QBO temperature
540 anomaly are varied. Precipitation also shows the greatest degree of variability between QBOE
541 and QBOW. Given that Son et al. (2017) found a strong QBO signal in precipitation based on
542 composites of the MJO in different QBO phases (their Figure 3), this lack of a clear signal is
543 difficult to reconcile with observations. However, Nie and Sobel (2015) found in their study
544 imposing similar QBO anomalies in an idealized model that the QBOE-QBOW precipitation
545 change was a non-monotonic function of sea-surface temperature. This non-monotonicity
546 resulted from a competition between changes in the gross moist stability (associated with

547 changes in the vertical structure of the large-scale vertical motion) and radiative feedbacks, and
548 suggests that precipitation changes may be more delicate than changes in other variables are.
549 Zhang and Zhang (2018) also looked more specifically at the question of the QBO influence on
550 MJO-related precipitation in their observational study. They noted that in the Indian Ocean,
551 QBO changes to total precipitation were insignificant due to cancelling effects of precipitation
552 associated with the MJO and non-MJO precipitation: non-MJO precipitation shows increases in
553 QBOE whereas MJO precipitation decreases in QBOE. These results, in conjunction with our
554 study, suggest the relationship between the QBO and MJO precipitation associated with the MJO
555 deserves more careful study.

556 Finally, based on observational evidence it is important to distinguish QBO changes to
557 tropical mean convection from QBO changes to convection associated with the MJO. Son et al.
558 (2017) showed that QBO changes to tropical mean OLR were not statistically significant,
559 whereas QBO changes to the variance of OLR on MJO timescales were significant (see their
560 Figure 1). As other studies have found evidence for QBO changes to mean convection (i.e.
561 Collimore et al. 2003; Liess and Geller 2012, Nie and Sobel 2015), more observational studies
562 on this nuance are needed. Still, in all our simulations in which the QBO has an influence on the
563 MJO, that influence is strongest during the MJO active phase and changes are smaller or have
564 the opposite sign during the suppressed phase. This strengthening primarily during the active
565 phase of the MJO leads to an increase in the variance on MJO time scales; whether the mean-
566 state changes depends on the relative sign and magnitude of changes during both the active and
567 suppressed phase.

568 In several of our runs, especially the 16km-peaked temperature experiment, we observe a
569 change in the time-mean of all the variables we consider, including OLR and precipitation. This

570 seems inconsistent with the results of Son et al. (2017). However, our 65-day time period of
571 integration makes comparison of the mean-state and the MJO time scales difficult to distinguish,
572 as only two active MJO phases and one suppressed phase are simulated. It may be that for longer
573 integrations that simulate more MJO events, as well as periods where no MJO is present, mean-
574 state changes like the observed would be averaged out.

575 Additionally, the 16km-peaked and 17km-peaked runs have a stronger QBO forcing than is
576 observed, making direct comparison with observations difficult. It may be that the strong
577 response in these cases during the MJO active phase overwhelm smaller changes during the
578 suppressed phase, leading to a change in the mean. In runs with smaller forcing, such as the
579 18km-peaked temperature experiments, the increase in the active phase is smaller, and is
580 balanced in the mean by the decreases during the suppressed phase, leading to less change in the
581 mean-state while still allowing for a change in variance (i.e. Figure 11).

582

583 **5. Conclusions**

584

585 In this study we examine the MJO-QBO relationship in a cloud-resolving model coupled to
586 parameterized large-scale dynamics. The goal is to explore whether the model can reproduce
587 aspects of the observed MJO-QBO relationship; in particular, a strengthening (weakening) of
588 MJO convection during the easterly (westerly) phase of the QBO. We also seek to identify likely
589 pathways through which the QBO modulates the MJO. After establishing that our model
590 reasonably reproduces two observed MJO events (Figure 3), we conduct three types of
591 experiments: (1) adding only QBOE/W temperature signals to our large-scale forcing; (2) adding
592 only QBOE/W wind signals; and (3) adding QBOE/W temperature and wind signals together.

593 These experiments were designed to isolate particular pathways of potential QBO influence. In
594 addition, we conducted sensitivity experiments modifying the height of the QBO anomalies, and
595 in the case of the temperature anomaly also changed the amplitude of the QBO forcing (see
596 Table 1). Our main results can be summarized as follows:

597 (1) Forcing the model with idealized QBO temperature signals in the tropopause region
598 (without the accompanying QBO wind anomalies) influences the simulated MJO events
599 in a manner qualitatively consistent with the observed MJO-QBO interaction:
600 strengthening of MJO convection during QBOE and weakening during QBOW (Figures
601 4-5). This relationship holds across several different variables, including cloud fraction,
602 vertical velocity, precipitation, and outgoing longwave radiation.

603 (2) QBO wind signals do not have a large effect on the model MJO (e.g. Figure 7). Adding
604 wind and temperature together confirms that the dominant signal is due to the
605 temperature effects.

606 (3) The MJO response to the QBO depends significantly on the height and amplitude of the
607 QBO temperature anomaly: higher altitude or smaller amplitude QBO temperature
608 anomalies lead to a weaker MJO response (e.g. Figures 8, 13). For “realistic” heights of
609 the QBO temperature anomalies the QBO influence on our simulated MJO events is
610 much less dramatic than in cases with lower-than-observed anomalies, and for some
611 variables (e.g. precipitation) the QBOE-QBOW difference is inconclusive (Figure 11).

612 Taken as a whole, our results suggest that the QBO-induced temperature anomalies may be
613 primarily responsible for driving the majority of the MJO-QBO interaction. However, our results
614 do not entirely explain the observed MJO-QBO relationships, and several caveats deserve further
615 study or clarification. First, the model MJO responds weakly to more realistic QBO temperature

616 forcing. For larger-than-observed forcing (i.e. lower altitude anomalies) the MJO response is
617 clear and qualitatively of the correct sign, but more realistic QBO temperature anomalies display
618 a much smaller signal that is difficult to detect. Additionally, the model's precipitation response
619 to the QBO is at times either absent or of the opposite sign than initially expected (i.e. is higher
620 during QBOW than QBOE). Precipitation also displays non-monotonic behavior in our
621 sensitivity testing and the response to the QBO is sensitive to the model configuration (Appendix
622 A). While some modeling and observational studies suggest this may not be entirely inconsistent
623 with observations (Nie and Sobel 2015; Zhang and Zhang 2018 others indicate a strong
624 precipitation signal (Son et al. 2017) making our results difficult to contrast with observations.
625 Finally, in several simulations in which the MJO response to the QBO is clearly seen, we
626 observe changes not only to the variance of convection, but also to the mean-state. This seems
627 inconsistent with the results of Son et al. (2017) and does not explain why MJO convection
628 seems affected more strongly by the QBO than climatological convection.

629 Additional work is needed to verify our results in other modeling studies, especially those
630 which simulate more complex pathways of QBO influence or a more realistic interplay between
631 the MJO and QBO. More specific hypotheses for the exact mechanism driving the MJO-QBO
632 relationship, as well as extensions of this study which increase the statistical robustness of our
633 results, will be explored in future work.

634

635 **APPENDIX**

636

637 **A1. Sensitivity to SWTG Top**

638 In this section we briefly examine the sensitivity of our results to the SWTG top
639 boundary condition and the vertical modes calculated from the N^2 profile (see Section 2.2). We
640 performed several QBO experiments with the SWTG modes recalculated with a rigid lid at 16km
641 rather than at 20km as in the above runs. While this lower lid is closer to the observed vertical
642 velocity in the DYNAMO data (see Figure 1 panel a), it may be overly restrictive in allowing the
643 vertical velocity to respond to anomalies that take place high the troposphere/in the stratosphere.
644 Here we show results from an experiment that is identical to the 16km-peaked temperature-only
645 run from Section 3.2 except for the changes to the modes/rigid lid.

646 Figure A1 shows the OLR and precipitation time series from these integrations. The
647 general sign and magnitude of QBOE-QBOW differences are not markedly different from the
648 higher lid cases in the vertical velocity and cloud fraction and thus are not shown. However, the
649 precipitation results no longer conclusively show an increase in rain during QBOE relative to
650 QBOW: note that during the first MJO event, there are periods where QBOE precipitates more
651 (e.g. ~ day 23 and ~day 29) and other periods (e.g. ~ day 33) where QBOW precipitates more.
652 The same is true for the second MJO event. This lack of consistency even within individual
653 events indicates that the precipitation response to the QBO in this model is sensitive to the details
654 of the model configuration and is less consistent than other variables showing an increase in
655 QBOE compared to QBOW.

656

657 **Acknowledgement**

658

659 The authors acknowledge support from NSF AGS-1543932.

660

661 **References**

662 Anber, U., S. Wang, and A. Sobel, 2017: Coupling with ocean mixed layer leads to intraseasonal
663 variability in tropical deep convection: Evidence from cloud-resolving simulations. *J. Adv.*
664 *Model. Earth Syst.*, **9**, 616-626, doi:10.1002/2016MS000803.

665
666 Baldwin, M.P., et al., 2001: The quasi-biennial oscillation. *Rev. Geophys.*, **39(2)**, 179-229, doi:
667 10.1029/1999RG000073.

668
669 Bergman, J., and P. D. Sardeshmukh, 2004: Dynamic stabilization of atmospheric single column
670 models. *J. Clim.*, **17**, 1004–1021, [https://doi.org/10.1175/1520-](https://doi.org/10.1175/1520-0442(2004)017<1004:DSOASC>2.0.CO;2)
671 [0442\(2004\)017<1004:DSOASC>2.0.CO;2](https://doi.org/10.1175/1520-0442(2004)017<1004:DSOASC>2.0.CO;2).

672
673 Bony, S., and K. A. Emanuel, 2005: On the role of moist processes in tropical intraseasonal
674 variability: Cloud-radiation and moisture convection feedbacks. *J. Atmos. Sci.*, **62**, 2770–2789,
675 <https://doi.org/10.1175/JAS3506>.

676
677 Chou, M.-D., and M. J. Suarez, 1999: A solar radiation parameterization for atmospheric studies.
678 NASA Tech. Rep. NASA/TM-1999-10460, vol. 15, 38 pp., NASA, Washington, D. C.

679
680 Collimore, C. C., D. W. Martin, M. H. Hitchman, A. Huesmann, and D. E. Waliser, 2003: On the
681 relationship between the QBO and tropical deep convection. *J. Clim.*, **16(15)**, 2552–2568,
682 [https://doi.org/10.1175/1520-0442\(2003\)016%3C2552:OTRBTQ%3E2.0.CO;2](https://doi.org/10.1175/1520-0442(2003)016%3C2552:OTRBTQ%3E2.0.CO;2).

683

684 Creuger, T., and B. Stevens, 2015: The effect of atmospheric radiative heating by clouds on the
685 Madden-Julian Oscillation. *J. Adv. Model. Earth Syst.*, **7**, 854–864, doi:10.1002/2015MS000434.
686

687 Daleu, C. L., et al., 2015: Intercomparison of methods of coupling between convection and large-
688 scale circulation. Part I: Comparison over uniform surface conditions. *J. Adv. Model. Earth Syst.*,
689 **7**, doi:10.1002/2015MS000468.

690

691 Daleu, C. L., et al., 2016: Intercomparison of methods of coupling between convection and large-
692 scale circulation: 2. Comparison over nonuniform surface conditions. *J. Adv. Model. Earth Syst.*,
693 **8**, 387–405, doi:10.1002/2015MS000570.

694

695 Dee, D. P., et al., 2011: The ERA-Interim reanalysis: Configuration and performance of the data
696 assimilation system. *Q. J. R. Meteorol. Soc.*, **137**, 553–597, <https://doi.org/10.1002/qj.828>.

697

698 Edman, J. P., and D. M. Romps, 2014: An improved weak pressure gradient scheme for single-
699 column modeling. *J. Atmos. Sci.*, **71**(7), 2415–2429, <https://doi.org/10.1175/JAS-D-13-0327.1>.

700

701 Edman, J. P., and D. M. Romps, 2015: Self-consistency tests of large-scale dynamics
702 parameterizations for single-column modeling. *J. Adv. Model. Earth Syst.*, **7**, 320–334,
703 doi:10.1002/2014MS000378.

704

705 Emanuel, K., A. A. Wing, and E. M. Vincent, 2013: Radiative-convective instability. *J. Adv.*
706 *Model. Earth Syst.*, **5**, doi:10.1002/2013MS000270.

707

708 Fulton, S. R., and W. H. Schubert, 1985: Vertical normal transforms: Theory and application.

709 *Mon. Weather Rev.*, **113**, 647–658, [https://doi.org/10.1175/1520-](https://doi.org/10.1175/1520-0493(1985)113<0647:VNMTTA>2.0.CO;2)

710 [0493\(1985\)113<0647:VNMTTA>2.0.CO;2](https://doi.org/10.1175/1520-0493(1985)113<0647:VNMTTA>2.0.CO;2).

711

712 Garfinkel, C. I., and D. L. Hartmann, 2011: The influence of the quasi-biennial oscillation on the

713 troposphere in winter in a hierarchy of models. Part I: Simplified dry GCMs. *J. Atmos. Sci.*,

714 **68(6)**, 1273–1289, doi:10.1175/2011JAS3665.1.

715

716 Giorgetta, M. A., L. Bengtsson, and K. Arpe, 1999: An investigation of QBO signals in the east

717 Asian and Indian monsoon in GCM experiments. *Climate Dyn.*, **15(6)**, 435–450,

718 doi:10.1007/s003820050292.

719

720 Gray, W. M., J. D. Sheaffer, and J. A. Knaff, 1992a: Hypothesized mechanism for stratospheric

721 QBO influence on ENSO variability. *Geophys. Res. Lett.*, **19(2)**, 107–110,

722 doi:10.1029/91GL02950.

723

724 Gray, W. M., J. D. Sheaffer, and J. A. Knaff, 1992b: Influence of the stratospheric QBO on

725 ENSO variability. *J. Meteor. Soc. Japan*, **70**, 975–995,

726 https://doi.org/10.2151/jmsj1965.70.5_975.

727

728 Hartmann, D. L., J. R. Holton, and Q. Fu, 2001: The heat balance of the tropical tropopause,
729 cirrus, and stratospheric dehydration. *Geophys. Res. Lett.*, **28**, 1969–1972,
730 doi:[10.1029/2000GL012833](https://doi.org/10.1029/2000GL012833).
731

732 Hendon, H. H., and S. Abhik, 2018: Differences in vertical structure of the Madden-Julian
733 Oscillation associated with the quasi-biennial oscillation. *Geophys. Res. Lett.*, **45**, 4419–4428,
734 <https://doi.org/10.1029/2018GL077207>.
735

736 Herman, M. J., and D. J. Raymond, 2014: WTG cloud modeling with spectral decomposition of
737 heating. *J. Adv. Model. Earth Syst.*, **6**, 1121–1140, doi:10.1002/jame.v6.4.
738

739 Holton, J.R. and R.S. Lindzen, 1972: An updated theory for the quasi-biennial cycle of the
740 tropical stratosphere. *J. Atmos. Sci.*, **29**, 1076–1080, [https://doi.org/10.1175/1520-](https://doi.org/10.1175/1520-0469(1972)029<1076:AUTFTQ>2.0.CO;2)
741 [0469\(1972\)029<1076:AUTFTQ>2.0.CO;2](https://doi.org/10.1175/1520-0469(1972)029<1076:AUTFTQ>2.0.CO;2).
742

743 Hong, S.-Y., Y. Noh, and J. Dudhia, 2006: A new vertical diffusion pack- age with an explicit
744 treatment of entrainment processes. *Mon. Weather Rev.*, **134**, 2318–2341,
745 <https://doi.org/10.1175/MWR3199.1>.
746

747 Hong, Y., G. Liu, and J.-L. F. Li, 2016: Assessing the radiative effects of global ice clouds based
748 on CloudSat and CALIPSO measurements. *J. Climate*, **29**, 7651–7674, doi:[10.1175/](https://doi.org/10.1175/JCLI-D-15-0799.1)
749 [JCLI-D-15-0799.1](https://doi.org/10.1175/JCLI-D-15-0799.1).
750

751 Hood, L. L., 2017: QBO/solar modulation of the boreal winter Madden-Julian oscillation: A
752 prediction for the coming solar minimum. *Geophys. Res. Lett.*, **44**, 3849–3857,
753 <https://doi.org/10.1002/2017GL072832>.
754

755 Iacono, M. J., J. S. Delamere, E. J. Mlawer, M. W. Shephard, S. A. Clough, and W. D. Collins,
756 2008: Radiative forcing by long-lived greenhouse gases: Calculations with the AER radiative
757 transfer models. *J. Geophys. Res.*, **113**, D13103, doi:10.1029/2008JD009944.
758

759 Johnson, R. H., and P. E. Ciesielski, 2013: Structure and properties of Madden–Julian
760 oscillations deduced from DYNAMO sounding arrays. *J. Atmos. Sci.*, **70**, 3157–3179,
761 <https://doi.org/10.1175/JAS-D-13-065.1>.
762

763 Johnson, R. H., P. E. Ciesielski, J. H. Ruppert, and M. Katsumata, 2015: Sounding-based
764 thermodynamic budgets for DYNAMO. *J. Atmos. Sci.*, **72(2)**, 598–622, doi:10.1175/jas-d-14-
765 0202.1.
766

767 Klemp, J. B., J. Dudhia, and A. D. Hassiotis, 2008: An upper gravity-wave absorbing layer for
768 NWP applications. *Mon. Weather Rev.*, **136**, 3987–4004, doi:10.1175/2008MWR2596.1.
769

770 Kuang, Z., 2008: Modeling the interaction between cumulus convection and linear gravity waves
771 using a limited-domain cloud system-resolving model. *J. Atmos. Sci.*, **65**, 576–591,
772 <https://doi.org/10.1175/2007JAS2399.1>.
773

774 Kuma, K.-I., 1990: A quasi-biennial oscillation in the intensity of the intra-seasonal oscillation.
775 *Int. J. Climatol.*, **10**, 263–278, doi:[10.1002/joc.3370100304](https://doi.org/10.1002/joc.3370100304).
776

777 Lee, J. C.K., and N.P. Klingaman, 2018: The effect of the quasi-biennial oscillation on the
778 Madden–Julian oscillation in the Met Office Unified Model Global Ocean Mixed Layer
779 configuration. *Atmos. Sci. Lett.*, 1-9, <https://doi.org/10.1002/asl.816>.
780

781 Li, X., Janiga, M. A., Wang, S., Tao, W.-K., Rowe, A., Xu, W., et al., 2018: Evolution of
782 precipitation structure during the November DYNAMO MJO event: Cloud-resolving model
783 intercomparison and cross validation using radar observations. *J. Geophys. Res. Atmos.*, **123**,
784 3530–3555. <https://doi.org/10.1002/2017JD027775>.
785

786 Liess, S., and M.A. Geller, 2012: On the relationship between QBO and distribution of tropical
787 deep convection. *J. Geophys. Res.*, **117**, D03108, <https://doi.org/10.1029/2011JD016317>.
788

789 Lindzen, R. S., and J. R. Holton, 1968: A theory of the quasi-biennial oscillation. *J. Atmos.*
790 *Sci.*, **25**, 1095-1107, [https://doi.org/10.1175/1520-0469\(1968\)025<1095:ATOTQB>2.0.CO;2](https://doi.org/10.1175/1520-0469(1968)025<1095:ATOTQB>2.0.CO;2).
791

792 Madden. R.A., and P.R. Julian, 1994: Observations of the 40-50-day tropical oscillation – A
793 review. *Mon. Wea. Rev.*, **122**, 814-837, doi: [10.1175/1520-](https://doi.org/10.1175/1520-0493(1994)122,0814:OOTDTP.2.0.CO;2)
794 [0493\(1994\)122,0814:OOTDTP.2.0.CO;2](https://doi.org/10.1175/1520-0493(1994)122,0814:OOTDTP.2.0.CO;2).
795

796 Mapes, B. E. and P. Zuidema, 1996: Radiative-dynamical consequences of dry tongues in the
797 tropical troposphere, *J. Atmos. Sci.*, **53**, 620-638, [https://doi.org/10.1175/1520-](https://doi.org/10.1175/1520-0469(1996)053<0620:RDCODT>2.0.CO;2)
798 [0469\(1996\)053<0620:RDCODT>2.0.CO;2](https://doi.org/10.1175/1520-0469(1996)053<0620:RDCODT>2.0.CO;2).

799

800 Mapes, B. E., 1997: What controls large-scale variations of deep convection?, in New insights
801 and approaches to cumulus parameterization. November 1996, 157–165, ECMWF workshop
802 proceedings, Reading, U. K.

803

804 Mapes, B. E., 2004: Sensitivities of cumulus ensemble rainfall in a cloud-resolving model with
805 parameterized large-scale dynamics. *J. Atmos. Sci.*, **61**, 2308–2317,
806 [https://doi.org/10.1175/1520-0469\(2004\)061<2308:SOCRIA>2.0.CO;2](https://doi.org/10.1175/1520-0469(2004)061<2308:SOCRIA>2.0.CO;2)

807

808 Marshall, A. G., H. H. Hendon S.-W. Son, and Y. Lim, 2017: Impact of the quasi-biennial
809 oscillation on predictability of the Madden–Julian oscillation. *Climate Dyn.*, **49(4)**, 1365–1377,
810 <https://doi.org/10.1007/s00382-016-3392-0>.

811

812 Matsui, T., W.-K. Tao, and J. J. Shi, 2007: Goddard radiation and aerosol direct effect in
813 Goddard WRF. NASA/UMD WRF Meeting, 14 Sep., Md.

814

815 Morrison, H., G. Thompson, and V. Tatarskii, 2009: Impact of cloud microphysics on the
816 development of trailing stratiform precipitation in a simulated squall line: Comparison of one-
817 and two-moment schemes. *Mon. Weather Rev.*, **137**, 991–1007, doi:10.1175/2008MWR2556.1.

818

819 Nie, J., and Sobel, A. H., 2015: Responses of tropical deep convection to the QBO: Cloud-
820 resolving simulations. *J. Atmos. Sci.*, **72(9)**, 3625–3638, [https://doi.org/10.1175/JAS-D-15-](https://doi.org/10.1175/JAS-D-15-0035.1)
821 [0035.1](https://doi.org/10.1175/JAS-D-15-0035.1).
822
823 Nie, J. and A. H. Sobel, 2016: Modeling the Interaction between Quasi-Geostrophic Vertical
824 Motion and Convection in a Single Column. *J. Atmos. Sci.*, **73**, 1101-
825 1117. <https://doi.org/10.1175/JAS-D-15-0205.1>.
826
827 Nishimoto, E., and S. Yoden, 2017: Influence of the stratospheric quasi-biennial oscillation on
828 the Madden–Julian oscillation during austral summer. *J. Atmos. Sci.*, **74(4)**, 1105–1125, doi:
829 <https://doi.org/10.1175/JAS-D-16-0205.1>.
830
831 Raymond, D. J., and X. Zeng, 2005: Modelling tropical atmospheric convection in the context of
832 the weak temperature gradient approximation. *Q. J. R. Meteorol. Soc.*, **131**, 1301–1320,
833 <https://doi.org/10.1256/qj.03.97>.
834
835 Romps, D., 2012a: Numerical tests of the weak pressure gradient approximation. *J. Atmos. Sci.*,
836 **69**, 2846–2856, <https://doi.org/10.1175/JAS-D-11-0337.1>.
837
838 Romps, D., 2012b: Weak pressure gradient approximation and its analytical solutions. *J. Atmos.*
839 *Sci.*, **69**, 2835–2845, <https://doi.org/10.1175/JAS-D-11-0336.1>.
840

841 Sentic, S., S. L. Sessions, and Z. Fuchs, 2015: Diagnosing convection with weak temperature
842 gradient simulations of DYNAMO. *J. Adv. Model. Earth Syst.*, **7**, doi:10.1002/2015MS000531.
843

844 Sessions, S., S. Sugaya, D. J. Raymond, and A. H. Sobel, 2010: Multiple equilibria in a cloud
845 resolving model. *J. Geophys. Res.*, **115**, D12110, doi:10.1029/2009JD013.
846

847 Shi, J. J., et al., 2010: WRF simulations of the 20–22 January 2007 snow events over Eastern
848 Canada: Comparison with in-situ and satellite observations, *J. Appl. Meteorol. Climatol.*, **49**,
849 2246–2266, <https://doi.org/10.1175/2010JAMC2282.1>.
850

851 Skamarock, W. C., J. B. Klemp, J. Dudhia, D. O. Gill, D. M. Barker, M. G. Duda, X. Huang, W.
852 Wang, and J. G. Powers, 2008: A description of the advanced research WRF version 3,
853 NCAR/TN-4751 STR, 125 pp., NCAR Tech. Natl. Cent. for Atmos. Res., Boulder, Colo.
854

855 Sobel, A. H., G. Bellon, and J. Bacmeister, 2007, Multiple equilibria in a single-column model of
856 the tropical atmosphere. *Geophys. Res. Lett.*, **34**, L22804, doi:10.1029/2007GL031320.
857

858 Sobel, A. H., and C. S. Bretherton, 2000: Modeling tropical precipitation in a single column. *J.*
859 *Clim.*, **13**, 4378–4392, [https://doi.org/10.1175/1520-0442\(2000\)013<4378:MTPIAS>2.0.CO;2](https://doi.org/10.1175/1520-0442(2000)013<4378:MTPIAS>2.0.CO;2).
860

861 Sobel, A. H., and E. D. Maloney, 2012: An idealized semi-empirical framework for modeling the
862 Madden-Julian oscillation. *J. Atmos. Sci.*, **69**, 1691–1705, [https://doi.org/10.1175/JAS-D-11-](https://doi.org/10.1175/JAS-D-11-0118.1)
863 [0118.1](https://doi.org/10.1175/JAS-D-11-0118.1).
864

865 Sobel, A. H., and E. D. Maloney, 2013: Moisture modes and the eastward propagation of the
866 MJO. *J. Atmos. Sci.*, **70**, 187–192, <https://doi.org/10.1175/JAS-D-12-0189.1>.
867

868 Sobel, A. H., S. Wang, and D. Kim, 2014: Moist static energy budget of the MJO during
869 DYNAMO. *J. Atmos. Sci.*, **71**, 4276–4291, <https://doi.org/10.1175/JAS-D-14-0052.1>.
870

871 Son, S.-W., Y. Lim, C. Yoo, H. H. Hendon, and J. Kim, 2017: Stratospheric control of Madden–
872 Julian oscillation. *J. Climate*, **30**, 1909–1922, doi:[10.1175/JCLI-D-16-0620.1](https://doi.org/10.1175/JCLI-D-16-0620.1).
873

874 Tulich, S. N., D. A. Randall, and B. E. Mapes, 2007: Vertical-mode and cloud decomposition of
875 large-scale convectively coupled gravity waves in a two-dimensional cloud-resolving model. *J.*
876 *Atmos. Sci.*, **64**, 1210–1229, <https://doi.org/10.1175/JAS3884.1>.
877

878 Wang, J., H.-M. Kim, E. K. M. Chang, and S.-W. Son, 2018: Modulation of the MJO and North
879 Pacific storm track relationship by the QBO. *J. Geophys. Res. Atmos.*, **123**, 3976–3992,
880 <https://doi.org/10.1029/2017JD027977>.
881

882 Wang, S., and A. H. Sobel, 2011: Response of convection to relative sea surface temperature:
883 Cloud-resolving simulations in two and three dimensions. *J. Geophys. Res.*, **116**, D11119,
884 doi:[10.1029/2010JD015347](https://doi.org/10.1029/2010JD015347).
885

886 Wang, S., A. H. Sobel, and Z. Kuang, 2013: Cloud-resolving simulation of TOGA-COARE
887 using parameterized large-scale dynamics. *J. Geophys. Res. Atmos.*, **118**, 6290–6301,
888 doi:10.1002/jgrd.50510.

889

890 Wang, S., A. H. Sobel, A. Fridlind, Z. Feng, J. Comstock, P. Minnis, M. Nordeen,
891 2015: Simulations of cloud-radiation interaction using large-scale forcing derived from the
892 CINDY/DYNAMO northern sounding array. *J. Adv. Model. Earth Syst.*, **7(3)**, 1472-1498,
893 doi:10.1002/2015MS000461.

894

895 Wang, S., A. H. Sobel, and J. Nie 2016: Modeling the MJO in a cloud-resolving model with
896 parameterized large-scale dynamics: Vertical structure, radiation, and horizontal advection of dry
897 air. *J. Adv. Model. Earth Syst.*, **8**, 121–139, doi:10.1002/2015MS000529.

898

899 Wu, Z., E. S. Sarachik, and D. S. Battisti, 2000: Vertical structure of convective heating and the
900 three-dimensional structure of the forced circulation on an equatorial beta plane. *J. Atmos. Sci.*,
901 **57**, 2169–2187, [https://doi.org/10.1175/1520-0469\(2000\)057<2169:VSOCHA>2.0.CO;2](https://doi.org/10.1175/1520-0469(2000)057<2169:VSOCHA>2.0.CO;2).

902

903 Yang, Q., Q. Fu, and Y. Hu, 2010: Radiative impacts of clouds in the tropical tropopause layer.
904 *J. Geophys. Res.*, **115**, D00H12, doi:10.1029/2009JD012393.

905

906 Yoneyama, K., C. Zhang, and C. N. Long, 2013: Tracking pulses of the Madden-Julian
907 oscillation. *Bull. Am. Meteorol. Soc.*, 1871–1891, doi: 10.1175/BAMS-D-12-00157.1.

908

909 Yoo, C., and S.-W. Son, 2016: Modulation of the boreal wintertime Madden-Julian oscillation by
910 the stratospheric quasi-biennial oscillation. *Geophys. Res. Lett.*, **43**, 1392-1398, doi:
911 10.1002/2016GL067762.

912

913 Zhang, C., 2005: Madden-Julian oscillation. *Rev. Geophys.*, **43**, RG2003,
914 doi:10.1029/2004RG000158.

915

916 Zhang, C., 2013: Madden–Julian oscillation: Bridging weather and climate. *Bull. Amer. Meteor.*
917 *Soc.*, **94**, 1849–1870, doi:[10.1175/BAMS-D-12-00026.1](https://doi.org/10.1175/BAMS-D-12-00026.1).

918

919 Zhang, C., and B. Zhang, 2018: QBO-MJO connection. *J. Geophys. Res. Atmos.*, **123**, 2957–
920 2967, <https://doi.org/10.1002/2017JD028171>.

921 **Tables and Figures**

Type	Height: z_0 (km)	Amplitude: $M_{u,t}$	Ensemble Size	Section
Control	--	--	5	3.1
Temperature	16	$\pm 1K$	5 QBOE&W	3.2
Temperature	17, 18, 19, 20	$\pm 1K$	1 QBOE&W per height	3.3.1
Temperature	18	$\pm 1K$	5 QBOE&W	3.3.1
Wind	18, 19, 20, 21, 22	10m/s & -15m/s	1 QBOE&W per height	3.3.1
Temperature and Wind	16/18, 17/19, 18/20, 19/21, 20/22	$\pm 1K$ +10m/s & -15m/s	1 QBOE&W per height	3.3.1
Temperature	16	$\pm .5K, \pm 2K$	1 QBOE&W per amplitude	3.3.2
16km Rigid Lid: Control	--	--	5	A1
16km Rigid Lid: Temp.	16	± 1	5 QBOE&W	A1

922

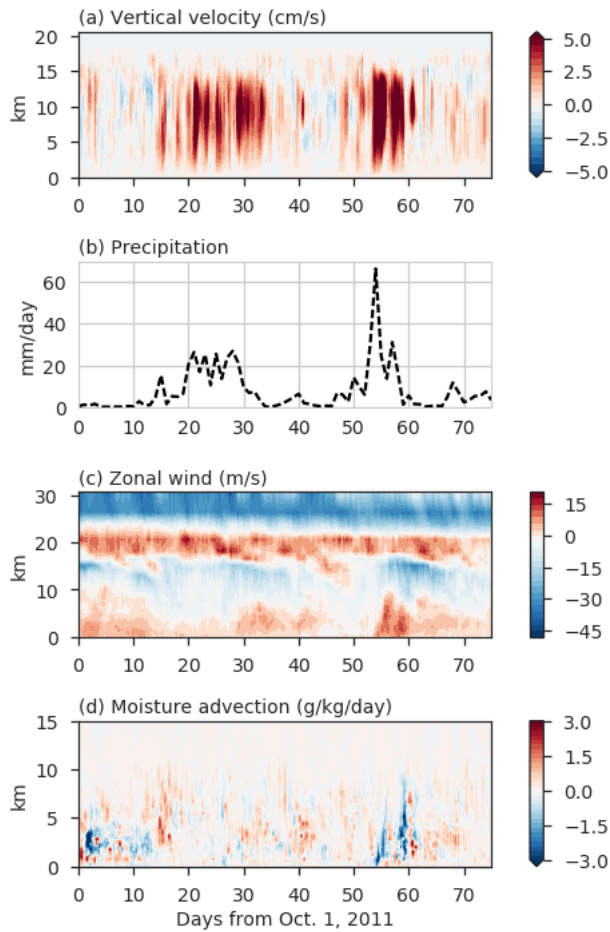
923 **Table 1.** List of experiments discussed in this paper. The first column indicates what type of
 924 QBO anomaly was imposed: control indicates no anomaly. The second and third column
 925 correspond to the height of the peak and its amplitude per Equation 2. Commas indicate separate
 926 experiments. For temperature and wind experiments, the height is listed in the form (temperature
 927 anomaly peak height/wind anomaly peak height). The fourth column lists the number of ensemble
 928 members: “QBOE&W” indicates the same number was used in for both QBOE and QBOW. The
 929 final column indicates the main section where the run is discussed.

List of experiments	Precipitation (mm/day)	OLR (W/m ²)
QBOE ($M_t = -2$ K)	7.51	165
QBOE ($M_t = -1$ K)	7.02	193
QBOE ($M_t = -0.5$ K)	6.50	203
Control	5.97	220
QBOW ($M_t = 0.5$ K)	5.76	224
QBOW ($M_t = 1$ K)	4.49	237
QBOW ($M_t = 2$ K)	3.98	243

930

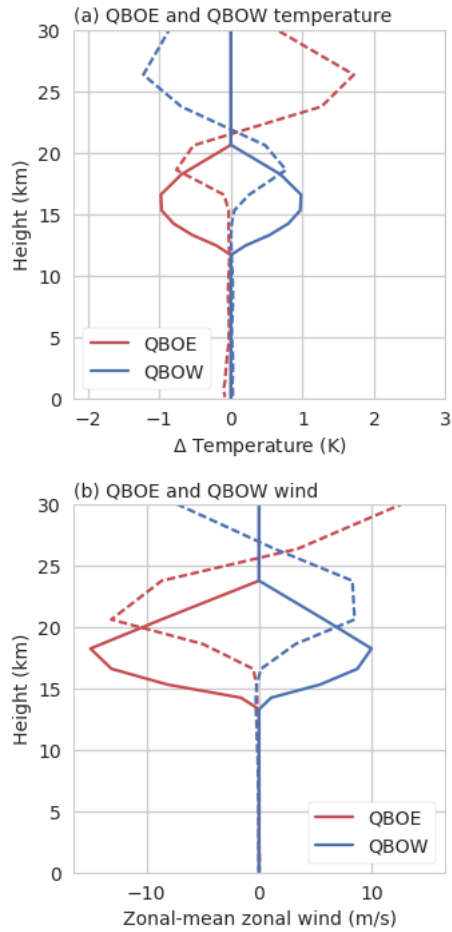
931 **Table 2.** Time-mean domain-averaged precipitation and outgoing longwave radiation for the
932 seven experiments varying the amplitude of the QBO temperature anomaly. The first column
933 indicates the amplitude of the QBO temperature anomaly, per Equation 2.

934



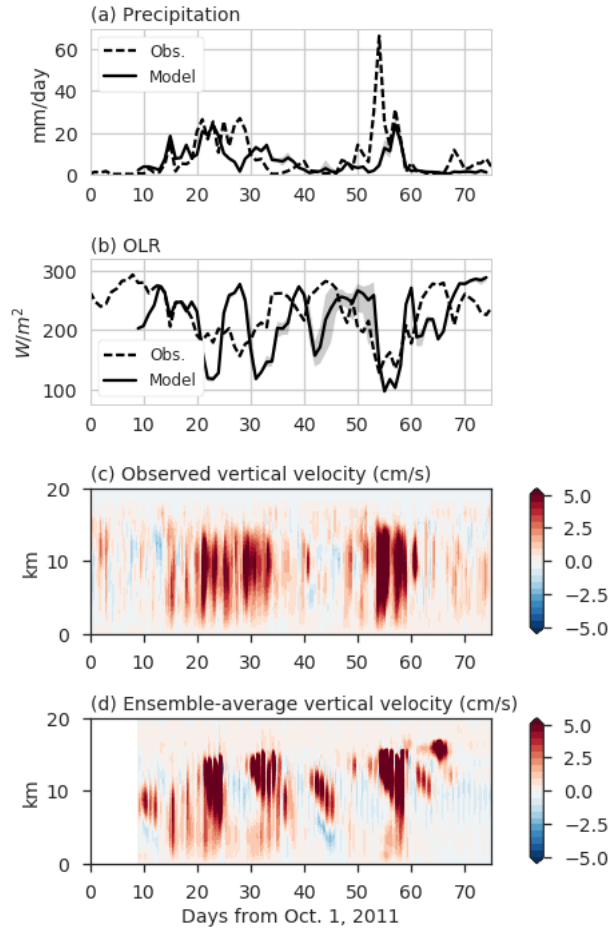
935

936 **Figure 1.** The DYNAMO/ERA-Interim linearly-merged data (as described in the text). Plotted
937 are (a) vertical velocity, (b) precipitation (from TRMM daily data), (c) zonal wind, and (d)
938 horizontal moisture advection. All fields are averaged over the DYNAMO Northern Sounding
939 Array, or in the case of ERA-Interim from 0-6°N and 73-80°E. Horizontal moisture advection is
940 plotted only up to 15km, as it is set to zero above that point per the text. Days are relative to
941 10/01/2011; the last day of the integration is 12/15/2011.



942

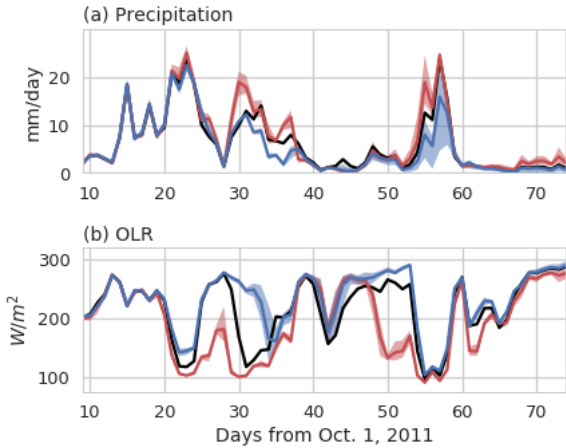
943 **Figure 2.** Idealized (solid) and observed (dashed), (a) QBO temperature and (b) wind anomalies
 944 averaged over the tropics (10°N to 10°S and all longitudes). The observed anomalies are
 945 calculated using a 50hPa QBO index based on ERA-Interim monthly data, as described in the
 946 text. The idealized anomaly is parabolic per Equation 2 in the text; here the peak is plotted at
 947 16km for the temperature anomaly and 18km for the wind anomalies, the lowest we extend the
 948 forcing. The idealized anomaly is plotted after interpolation onto the DYNAMO forcing levels,
 949 which do not have high resolution in the stratosphere, accounting for the vertical asymmetry
 950 about the peak in panel (b).



951

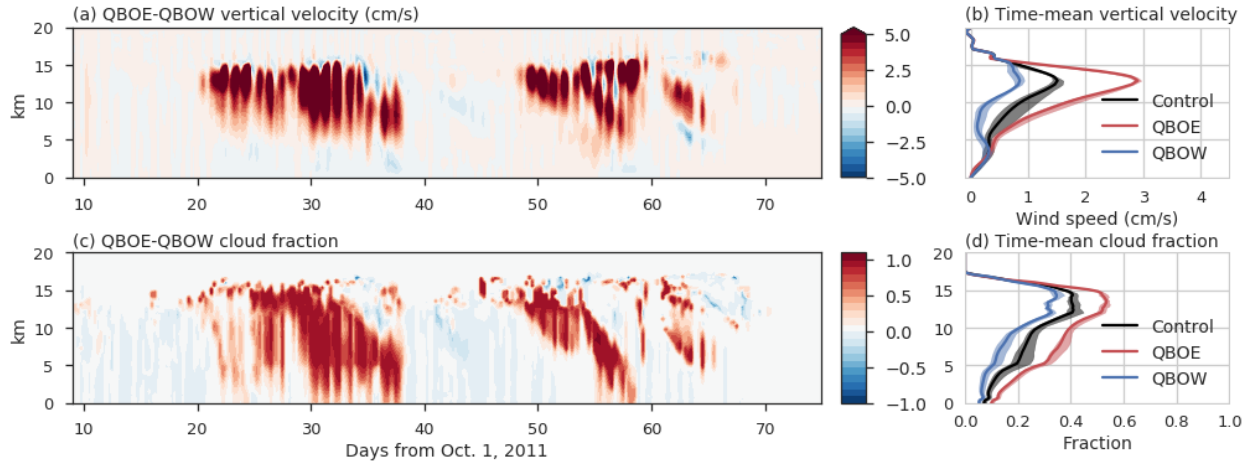
952 **Figure 3.** Control simulations compared to observations for (a) precipitation (mm/d), (b) OLR
 953 (W/m^2) and (c and d) vertical velocity (cm/s). In (a) and (b) shading denotes the spread among
 954 ensemble members, the bold black line is the model ensemble average and red line is the
 955 observed. For vertical velocity, the observations (c) over the DYNAMO NSA, and the model
 956 ensemble-averaged (d) is averaged horizontally over the model domain. The model is initialized
 957 on 10/10/2011 as described in the text; hence the white space preceding day 9.

958



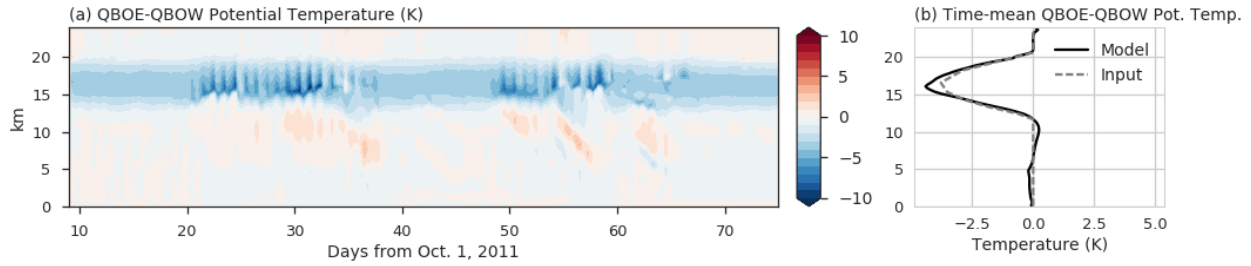
959

960 **Figure 4.** Precipitation (top) and OLR (bottom) from model integrations with no QBO anomaly
 961 (black), a QBOE temperature anomaly (red) and a QBOW temperature anomaly (blue). As
 962 before, the shading denotes ensemble members and the bold is the ensemble average; the spread
 963 in the control is not shown. The QBO temperature anomaly imposed in these runs peaks at $z_0 =$
 964 16 km with $M_t = \pm 1 K$ as shown in Figure 2 and described in the text. No QBO wind signal is
 965 added.



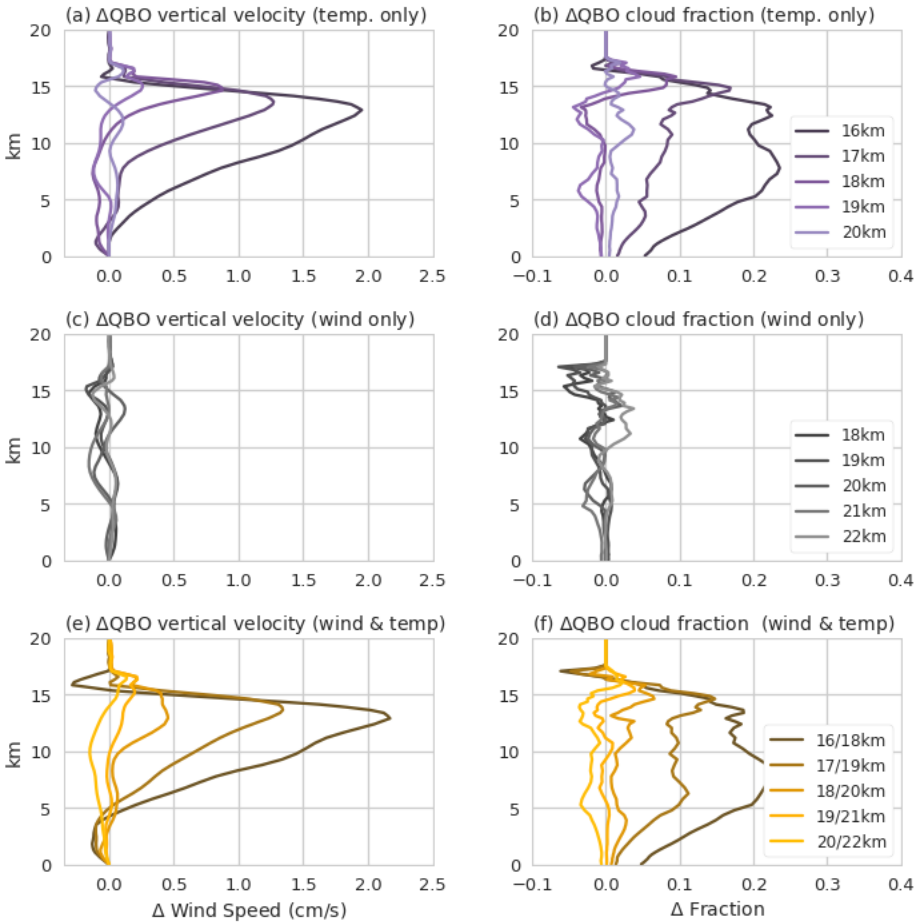
966

967 **Figure 5.** From the same QBO temperature experiment as in Figure 4, showing vertical velocity
 968 (top) and cloud fraction (bottom). The left panels are the QBOE-QBOW ensemble-averaged,
 969 horizontally-averaged difference (red indicates QBOE > QBOW). The right panels show the
 970 time-mean for QBOE, QBOW, and the control; the shading indicates ensemble spread. Here and
 971 throughout cloud fraction is calculated as the fraction of grid points with cloud-water content
 972 (cloud water vapor, ice, rain, snow, hail, and graupel) exceeding the minimum of .01 g/kg or 1%
 973 of its saturation value.



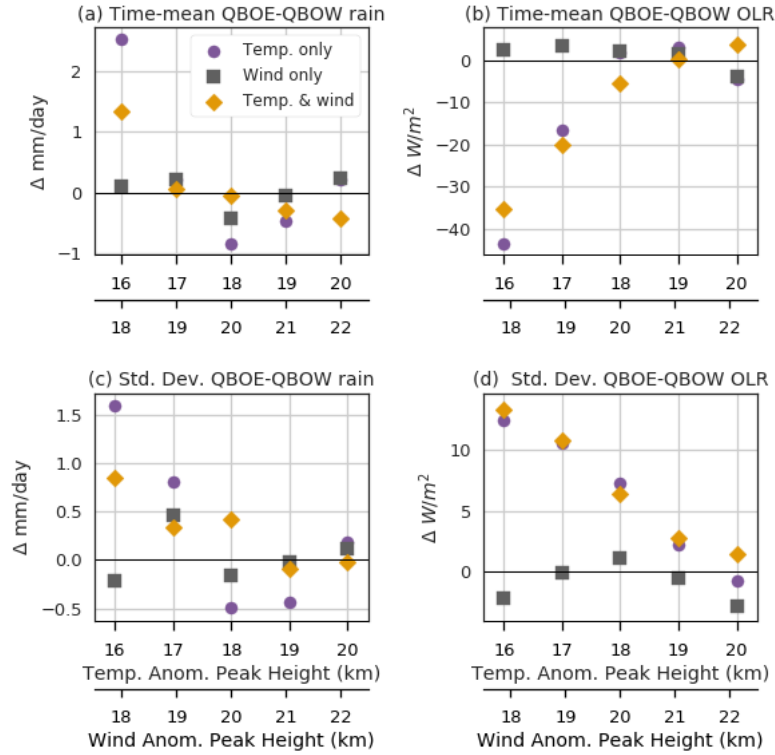
974

975 **Figure 6.** From the same QBO temperature experiment as in Figures 4 and 5, showing potential
 976 temperature difference in QBOE and QBOW. The left panel shows the difference between
 977 ensemble-averaged, horizontal averaged potential temperature. The right panel shows the time-
 978 mean difference (black, solid) as well as the idealized QBOE-QBOW temperature anomaly that
 979 is input into the model forcing (grey, dashed). Note here we plot potential temperature as
 980 opposed to temperature, which is shown in Figure 2. Results are shown up to the level where the
 981 model includes damping (24km).



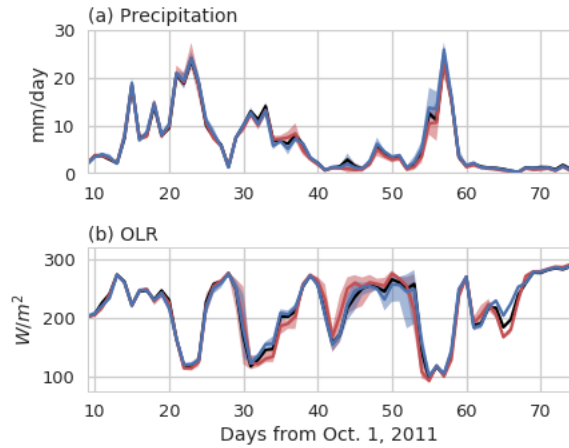
982

983 **Figure 7.** Time-mean, horizontal-mean QBOE-QBOW difference in vertical velocity (left) and
 984 cloud fraction (right). The top row are temperature-only experiments (purple), the center row are
 985 wind-only experiments (grey), and the bottom row are combined wind and temperature
 986 experiments (gold). Darker colors indicate lower-peaked anomalies; the legend indicates the
 987 altitude of the peak of the anomaly (z_0). For the combined temperature and wind experiments,
 988 the legend indicates first the height of the peak of the temperature anomaly, then that of the wind
 989 anomaly.



990

991 **Figure 8.** QBOE-QBOW differences in time-mean (top row) and standard deviation (bottom
 992 row) of rain (a,c) and OLR (b,d) from the same experiments as in Figure 7. The y-axis shows the
 993 magnitude of the difference. The x-axis is the altitude (in km) of the peak of the QBO
 994 temperature or wind anomaly: farther right corresponds to higher altitudes. The results are shown
 995 for temperature-only experiments (purple, circles), wind-only experiments (grey, squares), and
 996 temperature and wind experiments (gold, diamonds).



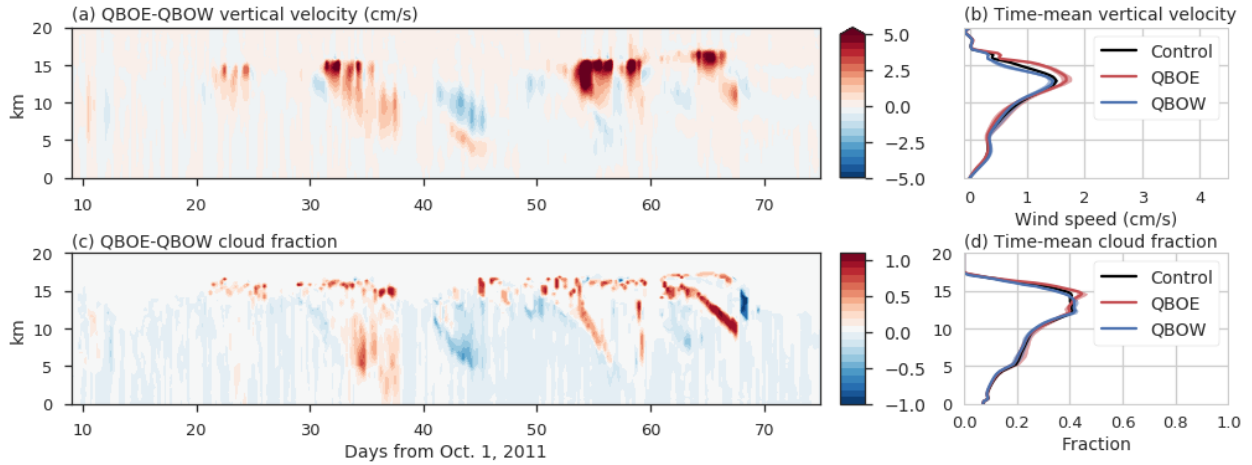
997

998 **Figure 9.** Horizontally-averaged precipitation (top) and OLR (bottom) from integrations with

999 QBO temperature anomalies which peak at 18km, as opposed to the 16km shown in Figure 4. As

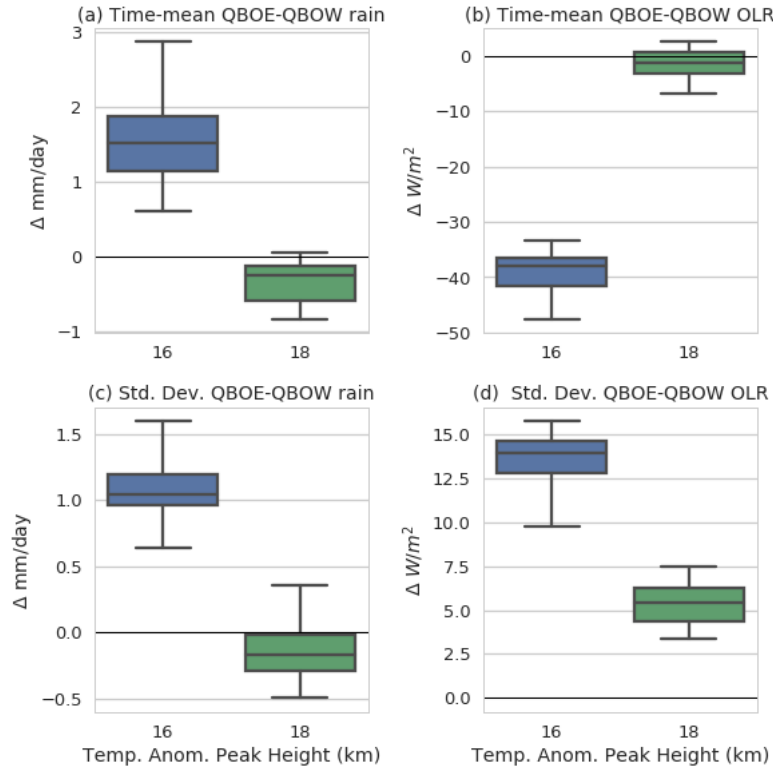
1000 in Figure 4, the shading indicates spread among ensemble members and the bold is the ensemble

1001 average; note that the control spread is not shown.



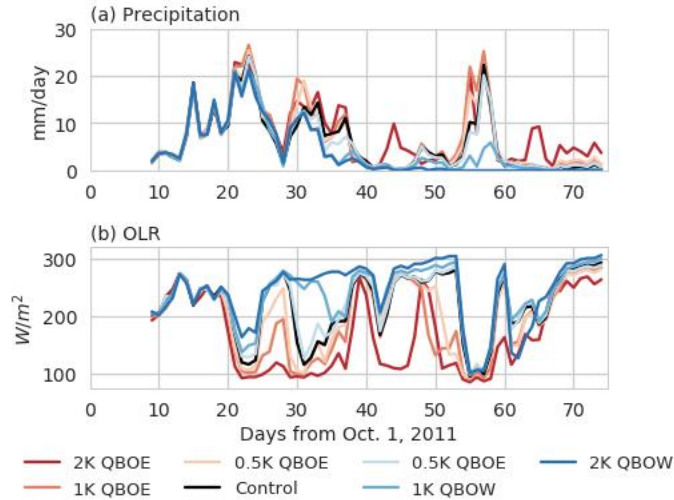
1002

1003 **Figure 10.** From the same experiments as in Figure 11, showing the horizontally-averaged,
 1004 ensemble-averaged QBOE-QBOW difference in vertical velocity (top) and cloud fraction
 1005 (bottom). As in Figure 5 right panels show the time-means for the control, QBOW, and QBOE
 1006 runs, with shading indicating ensemble spread.



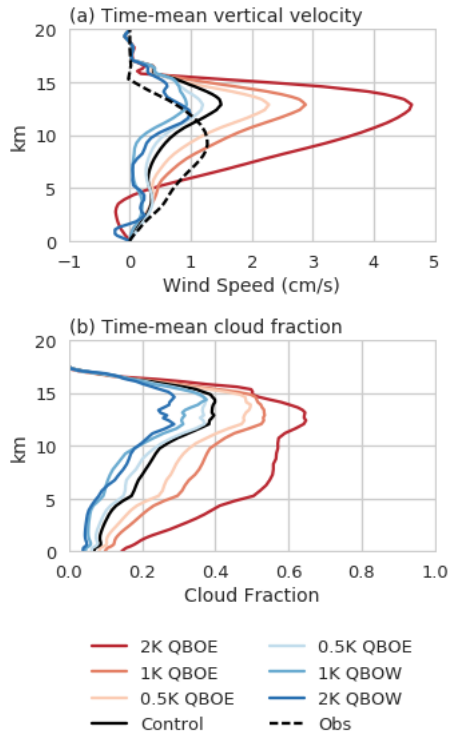
1007

1008 **Figure 11.** QBOE-QBOW changes in the mean (top) and standard deviation (bottom) of domain-
 1009 averaged rain (a,c) and OLR (b,d) in the 16km-peaked and 18km-peaked temperature
 1010 experiments. To capture the spread, the difference in the respective quantities was calculated for
 1011 all 25 pairs of the 5 QBOE and 5 QBOW ensemble members. The box plots mark the median
 1012 (center line), the upper and lower quartile (box).



1013

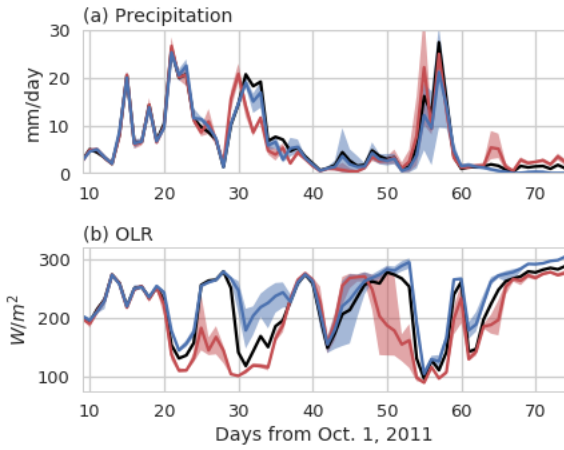
1014 **Figure 12.** Horizontally-averaged precipitation (top) and OLR (bottom) from simulations
 1015 changing the amplitude of the QBO temperature perturbation (the peak is fixed at 16km). Here
 1016 darker red shades indicate a stronger QBOE signal and darker blue indicates stronger QBOW
 1017 signal. The legend indicates the phase of the QBO and the magnitude of the QBO amplitude
 1018 ($|M_t|$). The control, 2K QBOE, and 2K QBOW runs are not the ensemble average as in Figure 4,
 1019 but a particular run chosen randomly from the five ensemble members, to better facilitate
 1020 comparison.



1021

1022 **Figure 13.** As in Figure 12; showing the time-mean vertical velocity and cloud fraction. The

1023 observed vertical velocity is also shown in dashed black.



1024

1025 **Figure A1.** As in Figure 4, but altering the spectral weak temperature gradient vertical modes
1026 and vertical velocity such that the model has a rigid lid at 16km, as opposed to the 20km rigid lid
1027 used elsewhere in this paper.











Click here to access/download
Non-Rendered Figure
Figure5.png











Click here to access/download
Non-Rendered Figure
Figure10.png



Click here to access/download
Non-Rendered Figure
Figure11.png





Click here to access/download
Non-Rendered Figure
Figure13.png



Click here to access/download
Non-Rendered Figure
FigureA1.png